Height reconstructions from geometric wavefronts using vision ray metrology

ANA HIZA RAMIREZ-ANDRADE[1] ![ORCID] AND **KONSTANTINOS FALAGGIS**[2,*] ![ORCID]

[1]*Department of Optical Science and Engineering, University of North Carolina at Charlotte, Charlotte, North Carolina 28223, USA*
[2]*Department of Mechanical Engineering and Engineering Sciences, University of North Carolina at Charlotte, Charlotte, North Carolina 28223, USA*
*kfalaggi@charlotte.edu

A recently reported vision ray metrology technique [Opt. Express **29**, 43480 (2021)] measures geometric wavefronts with high precision. This paper introduces a method to convert these wavefront data into height information, focusing on the impact of back surface flatness and telecentricity errors on measurement accuracy. Systematic errors from these factors significantly affect height measurements. Using ray trace simulations, we estimate reconstruction errors with various plano-concave and plano-convex elements. We also developed a calibration technique to mitigate telecentricity errors, achieving submicron accuracy in surface reconstruction. This study provides practical insights into vision ray metrology systems, highlighting validity limits, emphasizing the importance of calibration for larger samples, and establishing system alignment tolerances. The reported technique for the conversion of geometric wavefronts to surface topography employs a direct non-iterative ray-tracing-free method. It is ideally suited for reference-free metrology with application to freeform optics manufacturing. © 2024 Optica

1. INTRODUCTION

Many modern optical systems incorporate aspheric or freeform surfaces [1,2] to enhance performance in areas such as beam shaping for illumination and imaging applications [1–5]. To ensure that these manufactured surfaces align with their original design intent, metrology is needed for freeform surface manufacturing.

Interferometry provides accurate measurements for optics manufacturing but requires a reference (i.e., computer-generated holograms (CGHs) [6] or a spatial light modulator (SLM) [7] to produce an optical null.

Nevertheless, competitive freeform solutions need to be cost-effective, and the challenge in the case of metrology is that the costs are directly related to the measurement time and the complexity of the metrology solutions. High-end applications may justify costly solutions such as CGH-based interferometry or coordinate measuring machines (CMMs); however, for low-volume productions, this is not cost-effective. As a result, non-interferometric freeform metrology solutions continue to evolve. A popular technique is based on ray tracing for metrology in scenarios where the camera used for measurements can be accurately calibrated [8]. The null-screen methods [9–11] involve designing a set of geometric figures (the null-screen) which, upon reflection or refraction by a known optical surface (the reference), generates an image comprising regularly distributed circles or lines. Departures on the test surface with respect to the reference will change the spacing of the designed screen on the imaging plane, which is used with ray-tracing methods to estimate the characteristics of the test surface. Deflectometry [12–14] is another null-free approach that measures specular and refractive objects using ray tracing. The surface details are encoded on the change of sinusoidal fringe patterns displayed on a screen near the surface under test. Experimental ray tracing (ERT) [15] uses a single narrow, collimated beam that probes a surface, and the change in direction of the light ray is used to determine the surface properties. Inspired by this, the vision ray metrology approach [16] directly quantifies ray deflections, bypassing the need for a standard model and utilizing an optical setup that streamlines the reconstruction algorithms. Additionally, vision ray metrology routinely achieves 10 s of megapixel wavefront resolutions and, in principle, is only limited by the camera pixel count. This is a significant advantage when compared to Shack–Hartman Sensors (680 × 504 pixels) [17], or the Phasics wavefront sensor (360 × 416 pixels) [18]. This property allows vision ray metrology to highlight finer structures, i.e., mid-spatial-frequency (MSF) errors [16]. Furthermore, recent research has explored the application of vision ray solutions in other techniques [19,20] to reduce measurement errors. While initially designed for wavefront recovery [21,22], the vision ray metrology

approach offers distinct advantages over traditional deflectometry methods that require extensive calibration and optimization solvers [14,23,24]. For instance, the deflectometry system in [25] estimates surface profiles and pose parameters through a computational self-calibration approach using a stereo imaging system and ray tracing to model the measurement setup. In [26,27], the projection center of the imaging system is modeled as a point light source, necessitating precise alignment on the optical axis of the refractive element. Additionally, [26] requires ray tracing with a nominal surface model and knowledge of the sample-to-screen distance to calculate ray deflection. In contrast, [27] translates the screen to a second position and then optimizes the screen locations, assuming a planar surface. The computer-aided deflectometry approach in [24], combines coordinate measuring machine (CMM) measurements with optical software and numerical optimization to refine system geometry and reduce the systematic error. A second optimization determines coefficients defining the front and back surfaces of the refractive element as the superposition of an orthogonal basis using four measurements (front, back, 30 deg rotations around the xy axis). Similarly, this group had previously recovered effective wavefronts [14]. A detailed description of the calibration procedure that combines the initial geometrical parameters of the system (from a CMM), the ray-tracing model, and optimization is found in [28]. Nevertheless, the need for a CMM for calibration (e.g., after a thermal drift) significantly increases the system costs.

Motivated by that, this work proposes a new technique to convert the wavefront information recovered with vision ray metrology to height information from a plano lens without any additional change to the measurement setup and without the need for iterative optimization techniques.

This manuscript is structured as follows: Section 2.A introduces the surface reconstruction process of optical surfaces using vision ray metrology and its slope limitation. Section 2.B details the conditions used to test the impact of the flatness error on the plano side of the lens, as well as the telecentricity errors of the imaging system. The data processing technique is explained in Section 2.C. Sections 2.D–2.H provide simulation results to quantify the effect of systematic errors and assess the validity limits of the wavefront to height conversion. Discussions and conclusions are presented in Sections 3 and 4.

2. SURFACE RECONSTRUCTION USING VR METROLOGY

Vision ray metrology [16] measures wavefront from transmissive samples by quantifying the direction of the ray deflected by the sample, as shown in Fig. 1.

In VRM, every pixel of the imaging system of the VRM measurement system has a single vision ray assigned [8]. By employing ray tracing in reverse (see similar approach in deflectometry [12]), the properties of the sample under test can be described. Thus, every pixel that sees the sample is defined as a vision ray that passes through the sample (in jargon).

The sample is characterized by tracking the changes to the VRM line of sight (for each pixel) induced by the sample. This is achieved by keeping the distance between the sample and
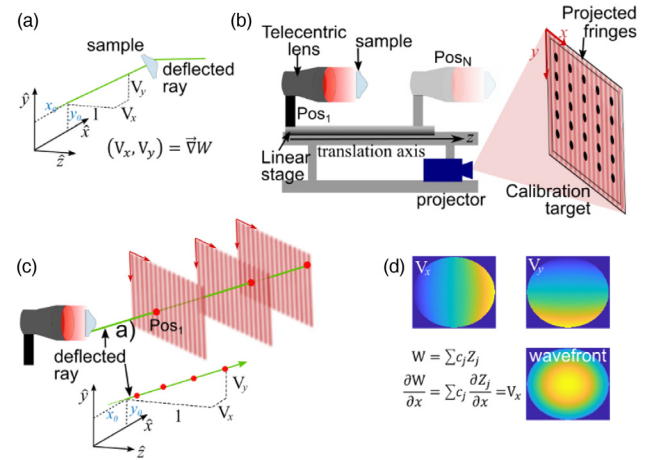

Fig. 1. Vision ray metrology. (a) Measurement principle. (b) Experimental setup. (c) Data collection, modeling, and fitting. (d) Measurement output.

imaging system constant and stepping the calibration target along the translation axis.

At each plane, the (x, y) coordinates of each vision ray are recovered. The final vision ray is then calculated by fitting a line in 3D space with the form of $\vec{r} = \vec{o}_c + z\vec{v}_c$, where $\vec{o} = [x_o, y_o]$ and $\vec{v}_c = [V_x, V_y]$ are the ray origin (offset) and the ray direction (slope), respectively. The values of (V_x, V_y) are then used to calculate the geometrical wavefront (W) using numerical integration [29], because they are related to the gradient of the geometric wavefront $\vec{\nabla} W$ as $\vec{\nabla} W = (V_x, V_y)$.

A. Surface Reconstructions Using VRM

To illustrate the principle of surface reconstructions with VRM, consider the case of Fig. 2, where an ideal telecentric imaging system (parallel rays) is used for VRM. In this setup, the sample has a perfectly flat surface on the sample's plano side and an unknown surface on the other side. This measurement configuration is used to estimate the height map based on the geometrical properties of the setup: once the vision rays ($\vec{V}_t$) of the imaging system (telecentric lens) are known, the sample-induced deflection is measured using the (x, y) coordinates ($\vec{q}$) that are gathered to find the direction of the deflected rays ($\vec{V}_s$). The vectors ($\vec{V}_t$) and ($\vec{V}_s$) are measured using the method in Ref. [16]. To compute the surface sag $h(x, y) = \Delta z$, we simply require the (x, y) coordinates ($\vec{q}$) at any given plane:

$$\vec{p} = \vec{q} + \Delta z \vec{V}_s = \Delta z \vec{V}_t + \vec{t}, \tag{1}$$

where for convenience we use the very first measurement plane, as shown in Fig. 2.

It can be seen that the surface sag detected by the pixel (u, v) at the sensor plane depends on (1) the change in the XY coordinates $(\vec{q} - \vec{t})$, and (2) the change in the direction $\vec{V}_t - \vec{V}_s$, seen by each pixel after the ray is deflected by the sample with respect to the telecentric image system. Solving this problem (for each pixel) is equivalent to a general regression problem $Ax = b$, with the matrix A and the vector b. Hence, the height can be calculated using Gaussian regression, $A^T A x = A^T b$, and for the following expression:
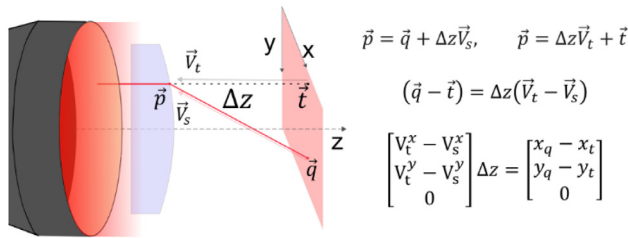
Fig. 2. Relationship between the vision rays of an ideal telecentric lens and the ray deflected from an optical element with a back-plano surface.

$$(\Delta V_x + \Delta V_y)\,\Delta z = (\Delta x + \Delta y)\,; \tag{2}$$

this leads to

$$\Delta z = (\Delta x \Delta V_x + \Delta y \Delta V_y) \big/ \big[(\Delta V_x)^2 + (\Delta V_x)^2\big], \tag{3}$$

which can be rewritten as

$$\Delta z = \langle \vec{s},\ \vec{V}\rangle / \|\vec{V}\|_2^2, \tag{4}$$

with $\vec{s} = [\Delta x,\ \Delta y]$ and $\vec{V} = [\Delta V_x,\ \Delta V_y]$.

These equations implicitly say that the front surface performs all refractive power, and the sag of the optical sample can be calculated directly. It should be noted that there is a fundamental slope limitation for the reconstruction. For the case of Fig. 2, where the flat surface needs to face the telecentric system, there is a limit for the maximum surface slope that can be measured. This limitation exists because, for large angles, the transmitted light from the target side does not match the acceptance angles of the telecentric system (<1 deg); see Fig. 1(b). The specific limit depends on the material's refractive index; a ray trace in reverse can be used to estimate this limit where the critical angle as a function of the refractive index gives the maximum slope that can be measured, as shown in Fig. 3.

Nevertheless, the previous approach has validity limits once systematic errors are considered. Examples are the sample back surface flatness or a non-perfect telecentricity of the imaging system. In the presence of those errors, the accuracy of the height maps is impacted.

The following sections analyze how the accuracy of the height measurement decreases as a function of the back surface flatness and the telecentricity to establish the limitation of this reconstruction method.
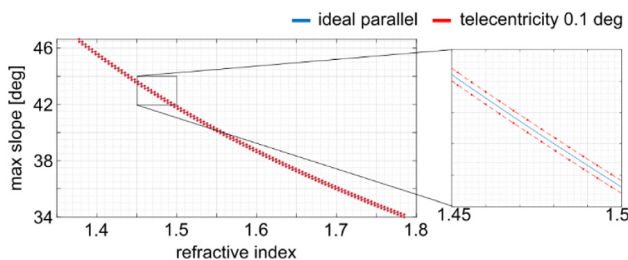

Fig. 3. Maximum slope by which the VRM can be measured using the approximation in Fig. 2.

B. Analysis of VRM Surface Reconstruction Techniques

This study uses ray trace in reverse simulations on FRED [30]. Multiple plano-concave and plano-convex elements from the Thorlabs catalog [31] have been used to estimate the error in surface reconstructions under more realistic conditions.

The flatness error is modeled as a superposition of the Zernike basis available in FRED. Two cases were modeled. Case I only considers the first 10 Zernike polynomials, and in Case II, the first 37 polynomials were used. (Simulations were performed using FRED version 22.40.4). The first 37 Zernike terms provide a reasonably comprehensive representation of various types of low-order aberrations that can occur in optical systems. The piston, tip, and tilt were not included. In this analysis, we have modeled different PV values of the back surface flatness to understand the error in the reconstruction of the front surface scales. Due to the nature of the ray trace in reverse, the imaging system was modeled using vision rays. For that purpose, we selected a 1″ CCD sensor with 20 MP resolution (3648 × 5472) on a FOV of ~115.7 mm (diagonal). We have also used the distribution of the vision ray parameter (x_o, y_o, V_x, V_y) of the telecentric lens that was measured in Ref. [16] with various maximum values of (V_x, V_y) to model two off-the-shelf telecentric systems (maximum telecentricity is 0.1 or 0.0123 deg). These cases, Case A and Case B, are shown in Fig. 4(c).

The overall study starts with a simulation to retrieve the surface reconstruction error when using Eq. (4) on data that only include the exemplary flatness errors for Cases I and II. Then the telecentricity is added using Cases A and B for the back surface error of Case I. Figure 5 shows an example of the data used for reconstruction. An overview is shown in Table 1. Subsequently, a comparison between the two telecentricity cases is performed to evaluate the influence of the telecentricity on the total reconstruction error. Then a calibration process is used to minimize the telecentricity errors. Furthermore, we consider sources of misalignment errors during the calculation of the
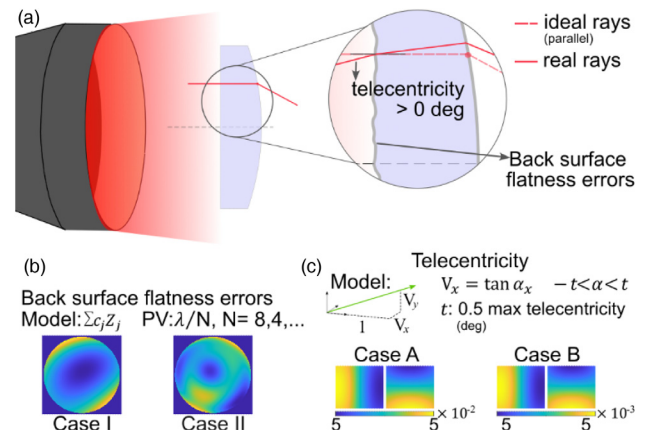

Fig. 4. Schematic of the systematic error studied: (1) flatness error of the back surface on the sample and (2) telecentricity of the imaging system. A ray trace in reverse was used for modeling: the imaging system is modeled as a source. (a) Flatness was modeled as a superposition of two arbitrary Zernike sets of coefficients. (b) Imaging system was modeled using the telecentricity specs from off-the-shelf lenses with a maximum telecentricity 0.0123 and 0.1 deg.
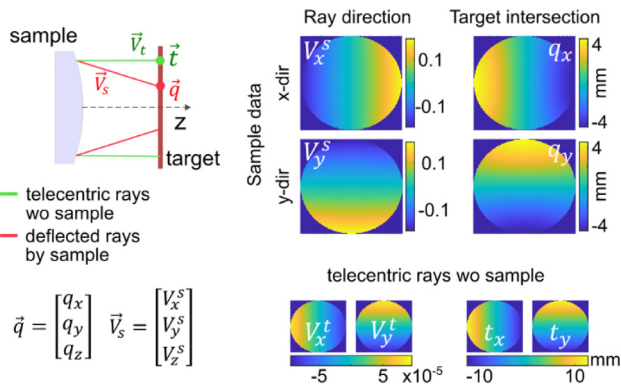
Fig. 5. Example of the data used for the reconstruction process on an arbitrary convex sample using Eq. (4).
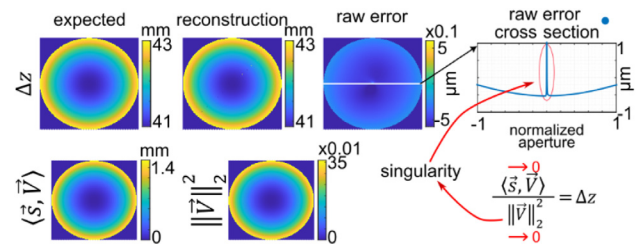

Fig. 6. Data used for reconstruction has a singularity region that produces a large error, as seen in its cross section. In this region, sample-induced deflection is diminutive; thus, $(\Delta y, \Delta x, \Delta V_x, \Delta V_y) \rightarrow 0$.

calibration parameter and quantify their impact, allowing us to provide guidelines to simplify the data processing and reduce the error in this case.

C. Data Processing

The height maps are reconstructed by applying Eq. (4) to every pixel on the telecentric systems that pass through the sample.

Close to the regions where the sample-induced deflections minimally change the direction of the rays $(\Delta y, \Delta x, \Delta V_x, \Delta V_y) \rightarrow 0$, the reconstruction is highly sensitive to errors. We refer to this area as the *singularity region*, as highlighted in Fig. 6. As can be seen from Eq. (4), this region is dominant in the center of the sample.

However, these points with $(\Delta V_x, \Delta V_y) \rightarrow 0$ can be masked out when applying an orthogonal basis decomposition. Alternatively, it is possible to apply a weighted fitting (giving less weight to points where $(\Delta V_x, \Delta V_y) \rightarrow 0$).

For simplicity, in this study, we removed data points so that we always kept at least 90% of the data, regardless of the sample aperture size. The mask is selected using a threshold based on the maximum value of $(\Delta V_x)^2 + (\Delta V_y)^2$, as shown in Fig. 7. The threshold used here was based on $||\vec{V}||_2^2$ using a value of $\min(100/||\vec{V}||_2^2)$.

D. Tests 1 and 2: Influence of the Presence of Back Surface Flatness Errors

The case of back surface reconstruction errors is analyzed in Tests 1 and 2 for a vast number of plano-concave and plano-convex surfaces with different radii of curvature (ROCs) and refractive indices. The results are shown in Fig. 8. The results show that the error decreases with an increasing aperture size. This is expected, assuming optics manufacturers can reliably produce a flatness of $\lambda/8$. This behavior can be highlighted by considering the case where the error from the back surface is the same when looking at normalized aperture sizes. When scaling the surface normalized coordinates (x_n, y_n) to the real coordinates, the slope is then proportional to $\partial z/\partial x$ or $(\partial z/\partial x_n)(\partial x_n/\partial x)$. If we double the aperture size, then the normalized aperture goes from $x_n = x/r$ to $x_n = x/2r$; thus, $(\partial x_n/\partial x)$ adds a factor of $1/2$. Hence, a larger aperture has a smaller slope, deflecting less the original vision rays.

Another result that can be extracted from Fig. 8 is that the error increases with the |ROC|. This behavior in the reconstruction error is explained by the relative error in $[\Delta V_x, \Delta V_y]$, which originates from the error in $\vec{V_t}$. Equation (4) assumes that $\vec{V_t}$ remains undisturbed until it reaches the front surface. This implies that the modulation of the rays is only assumed to be caused by the front surface. Nevertheless, the first surface does indeed refract the real $\vec{V_t}$. Furthermore, in real experiments, $\vec{V_t}$ are measured without the sample present; therefore, the error in $\vec{V_t}$ only depends on the back surface's flatness.

Table 1.   Overview of the Systematic Error Configuration for Each Test

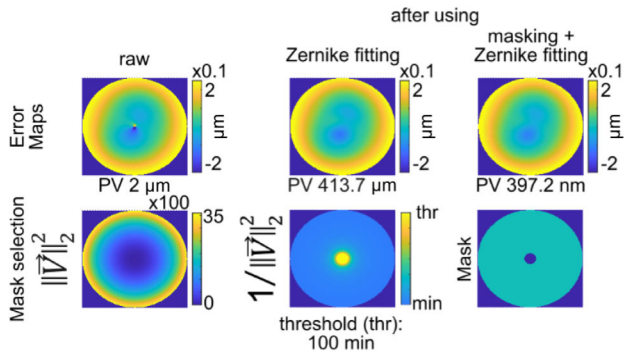|	Back Surface Flatness		Telecentricity			
	Case I	Case II	Case A	Case B		
Test No					Calibration	Section
1	1	N/A	N/A	N/A	N/A	2.D
2	N/A	1	N/A	N/A	N/A	2.D
3	1	N/A	N/A	1	N	2.E
4	1	N/A	1	N/A	N	2.E
5a	1	N/A	1	N/A	Y	2.F
5b	1	N/A	N/A	1	Y	2.F
6	N/A	N/A	N/A	1	1	2.G–2.H

Fig. 7. Singularity and its vicinity can be managed by (1) using a Zernike fitting on the raw data or (2) masking this region and then applying the Zernike fitting. For the mask selection, the points near the singularity region were removed entirely.

The samples with larger optical power have then a smaller relative error in ΔV_{xy}; see Fig. 9. Additionally, the singularity region where $(\langle \vec{s}, \vec{V} \rangle, ||\vec{V}||_2^2) \to 0$ influences the error in the center of the sample, because a larger |ROC| produced a smaller deflection of the vision rays, which results in a smaller $(\Delta V_x, \Delta V_y)$; see Fig. 9. The overall behavior is the same for both curvatures, but the error increases faster with the ROC for concave samples.

Another result of Fig. 8 is that the error caused by the normalized back surface flatness is more sensitive to the aperture size than to the |ROC|. When comparing the rate at which both variables increase the error, it becomes apparent that the error increases faster with a decreasing sample diameter than for an increasing |ROC|. An example is as follows: for a given sample with normalized back surface errors and a given ROC, we can expect a higher error if the diameter is decreased by half with the same ROC than for the same diameter but twice the ROC.

An important result is that, when considering only back surface errors, the reconstruction error of the front surface scales linearly with the PV of the back surface flatness. In other words,
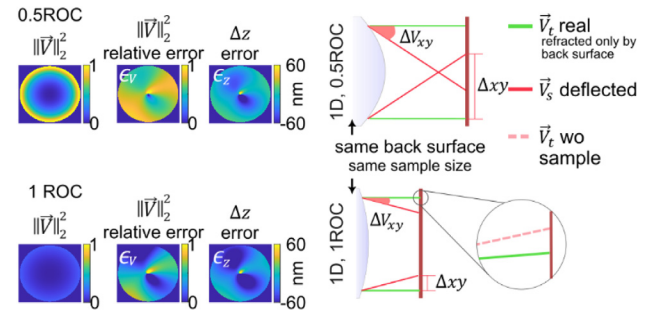

Fig. 9. Error increases with the |ROC|. For a pair of samples with the same aperture size but different ROCs, the relative error in the measured change of the ray direction increases with a larger ROC, since the sample deflects the rays in a smaller amount. For illustration purposes, $||\vec{V}||_2^2$ of two samples with the same D, and one ROC being a multiple of the other, was normalized and plotted on the same scale, similar to its relative error ϵ_V (independently, so the normalized magnitude of ϵ_V is not scaled with $||\vec{V}||_2^2$).

assuming a back surface flatness $S(x, y)$ with a PV error of λ/N produces a PV error of X, the double amount of back surface flatness errors (i.e., $2S(x, y)$) would produce a PV error of 2X. Many simulations verify this trend, as shown in Fig. 10.

E. Tests 3 and 4: Influence of the Presence of Back Surface Flatness Errors and Telecentricity Errors

In this section, the behavior of back surface reconstruction errors (Case I) is analyzed in the presence of telecentricity errors (Case A and Case B); the results are shown in Fig. 11.

Overall, for convex samples, the error still increases with the |ROC| independently of the refractive index and aperture size. However, there is an inflection point for the ROC/D ∼ 1, which is the case for slopes larger than ∼30 deg on the convex region (in our case, for $n = 1.43$, 1.38, 1.48, and 1.5). In the region where the error increases with a smaller |ROC|, the telecentricity completely dominates the error, while beyond
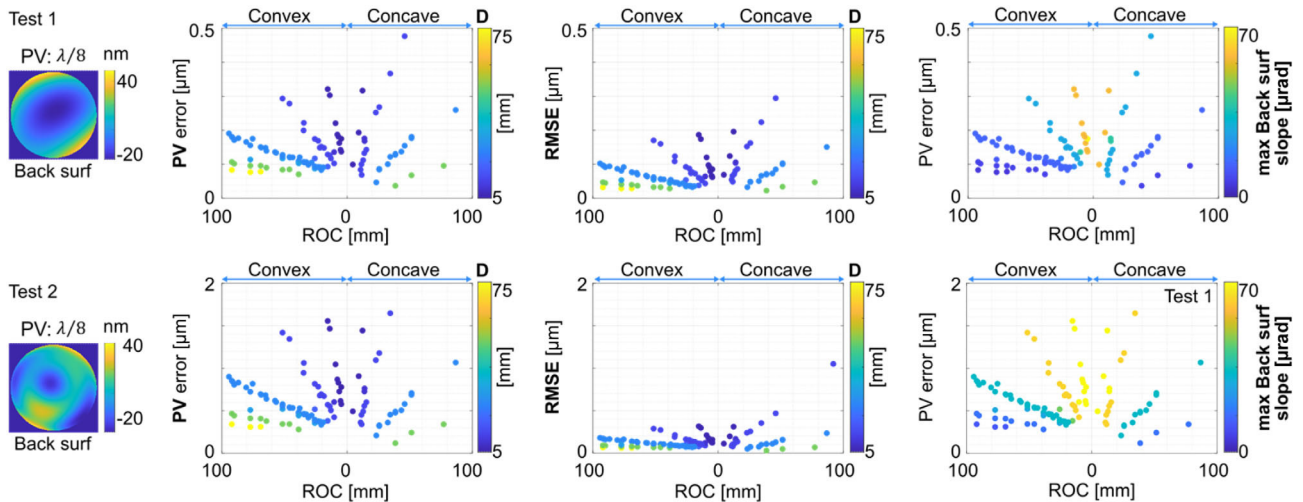

Fig. 8. (Tests 1 and 2) Error after reconstruction from Tests 1 and 2 (back surface flatness error only). The back surface flatness has a PV of $\lambda/8$ at 587 nm. The samples have an aperture size (D) from 5 to 75 mm (see color bars). The PV and RMS are plotted versus the ROC and D. The error decreases with D due to the back surface slope: a larger aperture has a smaller slope, and thus the error introduced from the refraction on the back surface is smaller. Test 2 has a larger back surface slope than Test 1, resulting in a larger error.
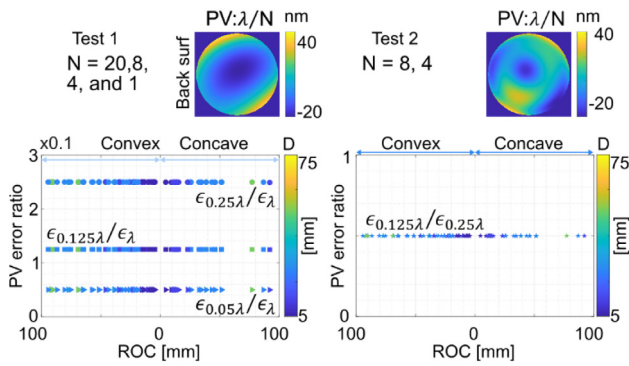
Fig. 10. (Tests 1 and 2) Error behavior for multiple PV values of the back surface flatness error for the same superposition of Zernike coefficients $S(x, y) = f\sum_{j=1}^{m} c_j Z_j$; the factor f is selected to produce a PV of λ/N, with N = 1, 4, 8, or 20. For Test 1, N = 1, 4, 8, and 20; for Test 2, N = 4, and 8. In all cases, the error scales linearly with the PV of the back surface flatness error independently from the sample's characteristics.
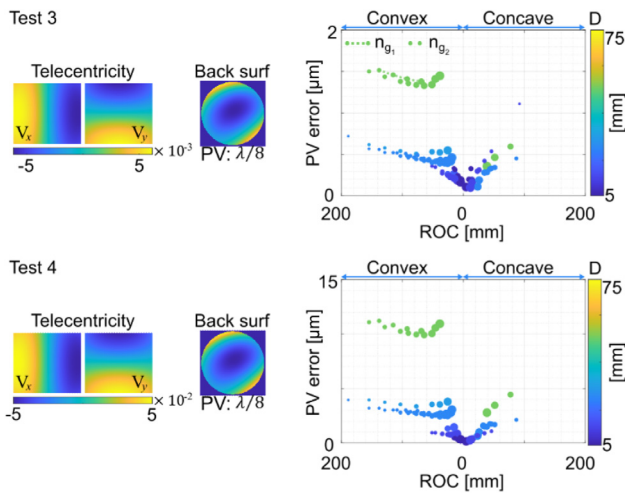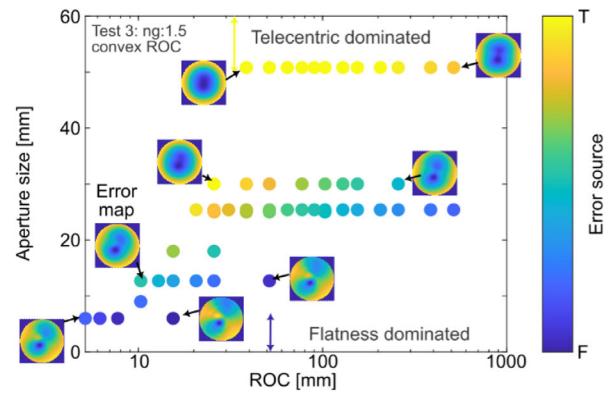

Fig. 12. (Test 3) Distribution of the primary source of error for the convex surface in Test 3. The telecentricity dominates the error toward the yellow color, resulting in defocus-like error maps. The color bar visualization was produced using a scaled product of the sample size, maximum sample slope and normalized defocus term of the error.
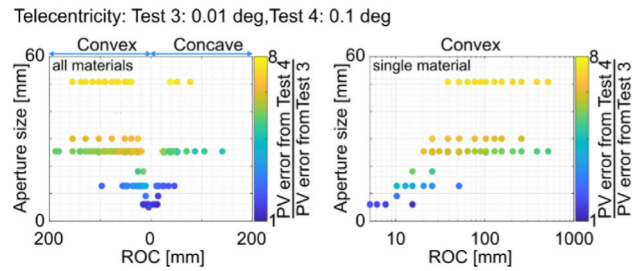

Fig. 11. (Tests 3 and 4) PVs of the error from Tests 3 and 4, when the back surface flatness (Case I) and the telecentricity are present during the reconstruction. The diameter of the dots in the graph is proportional to the maximum slope on the sample.

Fig. 13. (Tests 3 and 4) The ratio of the PV error from Test 4 and Test 3. The tests differ only in the telecentricity error, whereas Test 4 has a larger telecentricity error. A higher ratio value in these results indicates a larger influence of the telecentricity. In contrast, values ~ 1 show the error is minimally dependent on it (thus, the flatness error is dominant, and there is minimal change), which agrees with the figure of merit shown in Fig. 12.

that inflection point (i.e., at a larger |ROC|), the error results from both the back surface flatness and the telecentricity. (This agrees with the behavior observed in Figs. 12 and 13.) In regions where the influence of the telecentricity is larger, the slope of the function $PV_e(|ROC|)$ is smaller, since the telecentricity *dampens* the error of the back surface flatness. Thus, larger values of the telecentricity errors further decrease the impact of the back surface flatness error, resulting in a minimal change with an increasing |ROC| as is the case for the results of Test 4 (shown in Fig. 11).

The local oscillations of the PV for each D as function |ROC| are dependent on the refractive index. A larger refractive index gives a smaller error. For the same aperture size and comparable ROC, the material with a larger refractive index bends the rays more; a larger bend means a smaller relative error in ΔV_{xy}.

Figure 11 also shows that the error increases for larger values of D. This is in contrast to the case when only flatness errors

are present. Thus, telecentricity errors are responsible for this behavior. This effect is explained by the fact that the telecentric lenses have a ray divergence that increases as the distance from its optical axis increases; in other words, the angular span of the rays that intersect the sample is larger, as shown in Fig. 14.

Notably, when looking at the results of Test 3, the value of the ROC for which the telecentricity dominates the error depends on the sample aperture size. For Test 4, the telecentricity dominates all samples, except those with D < 10 mm.

It is also interesting to notice that when the telecentricity dominates the error, the reconstruction error appears to have a strong presence of a systematic defocus term. In the other cases, the error maps resemble the back surface slope, as seen in Fig. 12.

Preliminary modeling of the system's telecentricity errors on a large pool of samples can help understand if the errors need to be calibrated depending on the aimed reconstruction accuracy. When comparing the results from Tests 3 and 4, as done in Fig. 13, we see that for small samples with the aperture size < 0.1 × FOV of the imaging system the telecentricity does not influence the reconstruction.

These simulations also reveal that in the presence of the telecentricity error, the linearity of the reconstruction error with
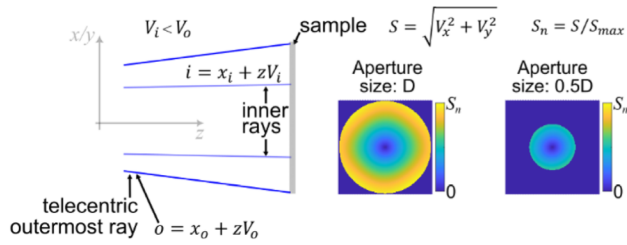
Fig. 14.   Acceptance angle of the telecentric system increases for pixels farther from the optical axis. For larger samples, the pixels observing the outermost part of the sample have larger acceptance angles or incidence angles on the sample back surface (when ray tracing in reverse).
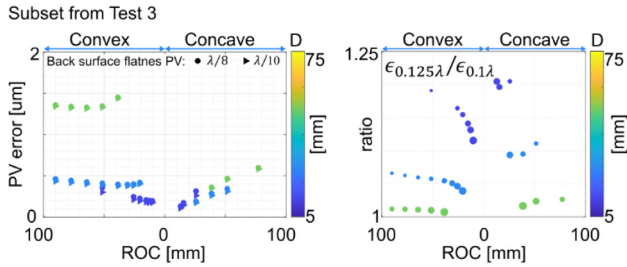

Fig. 15.   (Test 3) Comparison of the accuracy of the reconstruction on a single material and a few aperture sizes (2″, 1″, and 0.5″) for the same structure on the back surface flatness (Case I) but different PVs: $\lambda/8$ and $\lambda/10$. Once telecentricity is introduced, the error loses linearity with the flatness error, and the behavior is dependent on the aperture size.

respect to the back surface slope is lost, as shown in Fig. 15. This is different from the case of Fig. 10.

Notably, telecentricity error affects convex samples more rapidly than concave elements with an increasing |ROC| since the relative error in the real deflected rays is greater for convex samples than for concave samples due to the change of diverging rays to converging rays as shown in Fig. 16. For Fig. 17,
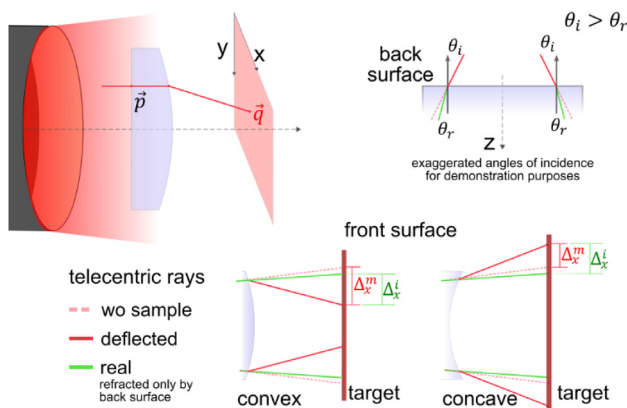

Fig. 16.   Diagram explaining the reason behind the larger error on convex samples for larger aperture sizes (for cases where the telecentricity dominates the error). The relative error in Δxy on the convex samples is larger than that for concave samples once the telecentricity is considered: the ideal value of Δ_{xy}^i is larger than the measured value Δ_{xy}^m in concave samples. This effect is reduced once the incidence angle of the outmost rays that pierces the sample is smaller (as the sample decreases). In this case, the difference in the error between the concave and convex samples also decreases.
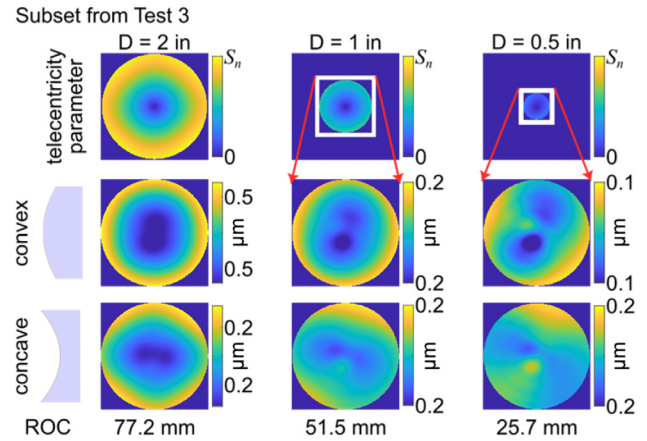

Fig. 17.   (Test 3) Error map comparison between three aperture sizes (2″, 1″, and 0.5″) for the same structure on the back surface flatness (Case I) with the PV: $\lambda/8$. The defocus term is an effect of the influence of the telecentricity on the imaging system; for smaller samples where the flatness of the back surface dominates, the error shows the impact of the back surface slope and the singularity region.

we elected the samples such that the |ROC| is larger for both curvatures, which is the case when the error is maximum for the concave samples, as seen in Fig. 15. This helps identify the major contributor to the error from the reconstruction.

F. Test 5: System Calibration to Compensate for Telecentricity Errors

The telecentricity errors of the imaging system add a defocus-like error term, as seen in Fig. 18, thus removing a sphere with a different radius of curvature, such that the nominal is not enough to reveal the deviations from the nominal shape of the sample. Consequently, calibration is necessary to minimize reconstruction errors.

In this work, we report a new calibration technique that applies to industrial practice, where time-efficient but still accurate solutions are needed. The telecentricity can be calibrated to minimize the error such that it only depends on the back surface flatness of the sample under test; here we take a Tikhonov regularization-like approach, and we estimate the surface as

$$\Delta z = \langle \vec{s}, \vec{V} \rangle / \left[\| \vec{V} \|_2^2 + \lambda \right]. \tag{5}$$
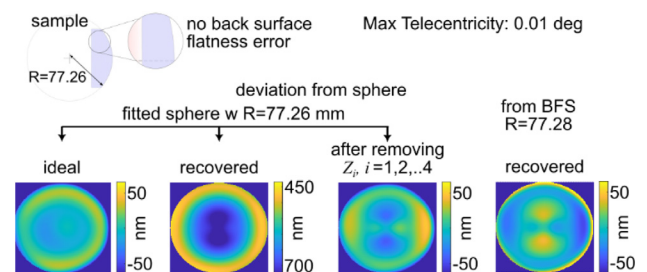

Fig. 18.   (Test 5) Comparison between the ideal and the reconstructed deviations from the sphere of a 1″ convex sample with the ROC = 77.26 mm. The back surface of the sample is perfectly flat. The telecentricity adds a piston, spherical, and other low-order terms to the reconstruction.
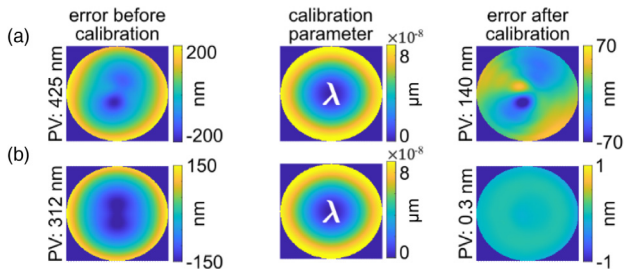
Fig. 19. (Test 5) Calibration of the telecentricity for a 1″ diameter BK7 sample. (a) Sample has a back surface flatness and telecentricity as in Test 3. (b) Sample has a perfectly flat back surface and telecentricity as in Test 3. The calibration parameter was obtained from the sample model (neither flatness errors on the back surface nor front surface deviation from the perfect sphere are considered).
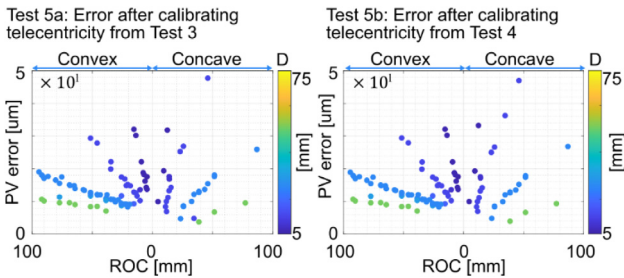

Fig. 20. (Test 5) Error after calibrating the telecentricity of the imaging system used in Tests 3 and 4. The calibration parameter was found from ideal conditions.

The calibration parameter λ can be found by first recovering the telecentric vision rays and performing a ray tracing of the measurement system model with similar geometrical parameters as the actual system, and then using a model of the tested element (with nominal parameters) to find λ for each pixel such that the cost function $f(\lambda)$ in Eq. (6) is minimized:

$$f(\lambda) = \Delta z_{\text{model}} - \langle \vec{s}, \vec{V} \rangle / \left[\|\vec{V}\|_2^2 + \lambda \right]. \qquad (6)$$

The main difference between this approach and similar methods is that we optimized only a single parameter for each pixel (2D λ map) instead of modeling the system's aberrations. Hence, this overcomes the need for sophisticated and iterative ray-tracing-based calibration methods. Instead, we generate this 2D λ map from a model of the reference sample (e.g., the prescription or the CAD model). This 2D λ map is robust against deviations from its ideal value due to misalignments and enables the vision ray metrology technique to measure errors that originate during manufacturing.

When using this calibration approach, it is possible to reduce the error to the case where only the back surface flatness is present, as shown in Fig. 19(a). For comparison, for the ideal case, where the back surface of the sample is perfectly flat, the error is below 1 nm, as shown in Fig. 19(b).

It should be noted that after calibration, the results from Tests 3 and 4 return to the same PV error levels as those found on Test 1 (see Figs. 20 and 8 for comparison), i.e., telecentricity errors are fully overcome.

The calibration parameter depends on the geometrical arrangement, specifically the sample location relative to the imaging system and screen. The direction of the vision rays of the deflected vision rays depends on the incident angle on the first surface; thus, the calibration parameter depends on the relative location of the sample with respect to the imaging system, z_{is}. For a given z_{is}, although the direction of the rays does not change (meaning the error in ΔV_{xy} is constant), the xy coordinates seen by each pixel are dependent on the target location (z_{st}). Thus, the calibration parameter is a function of these two distances, $\lambda = f(x, y, z_{is}, z_{st})$.

In the next section, we determine the dependency between the reconstruction error and the calibration parameter sensitivity using simulations to assess the effects of axial and lateral displacement errors on system configuration.

G. Test 6a: Analysis of Axial Sample and Target Misalignments on the Calibration Parameters

To identify the contribution of the error on the location of the sample while calculating λ, we select only a subset of the samples used in previous tests. Additionally, these samples have a perfectly flat back surface, and we investigate a ± 1 mm axial error during the simulations. This assumption is reasonable because, as discussed in Ref. [32], *"table top optomechanical mounts usually rely on visual alignment . . . it could be reasonably assumed that it is possible to center at resolution of 1/20th of the clear aperture of the optomechanical mount without any special tooling. This corresponds to about ± 1 mm for a 25.4 mm diameter lens mount."*

We have seen that the reconstruction error is larger with an increasing sample aperture size; however, a single axial error during the calibration parameter of ± 1 mm produces less than a 50 nm PV error in the reconstructed surface, even for 2″ samples for the smallest telecentricity of 0.0123 deg, as seen in Fig. 21.

For simplicity, we performed the same study for the imaging system with a larger telecentricity (i.e., maximum: 0.1 deg) for the sample with the largest error shown in Fig. 21, (D/ROC: 2″/38.6 mm) with $\epsilon z_{it} = 50$ mm, because it represents the largest reconstruction error. In this configuration, the errors are <400 nm.

H. Test 6b: Analysis of Lateral Sample Misalignments on the Calibration Parameters

Placing the sample at an off-center position induces an asymmetry in the reconstruction that prevents a proper surface fitting. The asymmetry can be removed by applying a tilt and offset to the recovered raw data before applying Eq. (4) for the reconstruction; this is shown in Fig. 22. However, this implies that extra steps need to be taken to calculate the calibration parameter λ (i.e., find the location of the sample and include this during the modeling of the system).

For simplicity, we suggest keeping the sample as close to the on-axis location as possible to avoid dealing with this extra step and then applying the calibration parameter from on-axis models. Off-the-shelf manual XY translation stages easily allow 10 μm resolution (e.g., Thorlabs ST1XY); here we tested 30 μm radial decentering. The error from the system without telecentricity calibration, Fig. 23, shows an error change of less than 5%, regardless of the sample size and maximum slope.
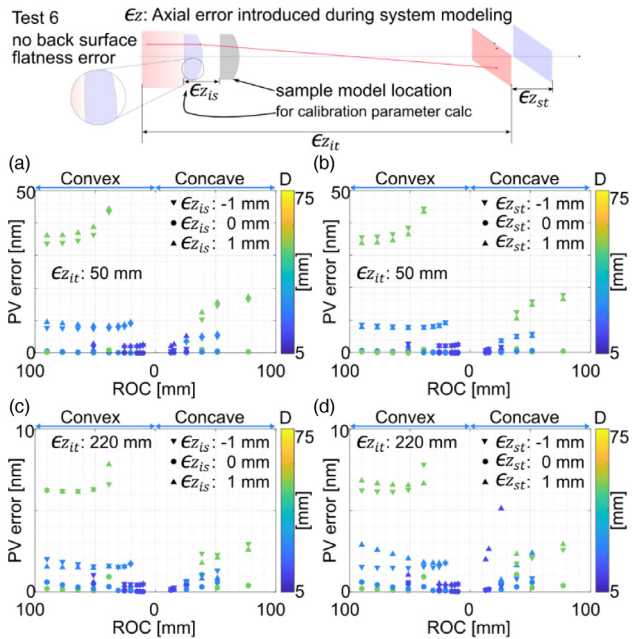
Fig. 21. (Test 6a) Effect of axial errors on the calibration parameter for 0.0123 deg maximum telecentricity. The pair telecentric/sample is at (ϵz_{it}) 50 mm in (a) and (b), or 220 mm from the target in (c) and (d). (a) and (c) Distance between the imaging system and the target is constant; only the lens location is modeled to have an error along the z axis. (b) and (d) Error along the z axis is modeled only on the target location.
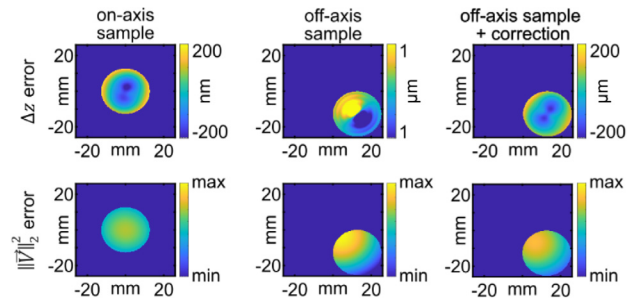

Fig. 22. (Test 6b) Comparison of the error for a convex 1″ diameter BK7 sample when measured the on- and off-axis. The center of the samples was translated off-axis radially ∼12.7 mm. An extra step needs to be taken before calibrating the telecentricity: set the pixel at the center of the sample as the optical axis of the imaging system to the origin of the measurement coordinate system.
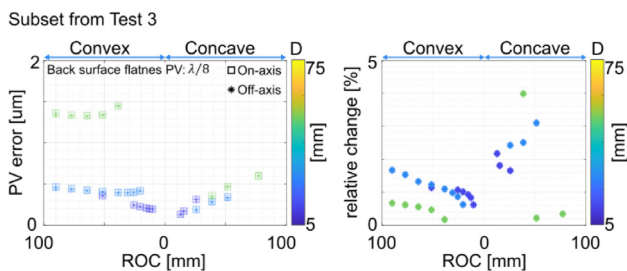

Fig. 23. (Test 6b) Comparison between the on-axis and off-axis samples. The center of the samples was moved off-axis radially ∼30 μm (∼1.7 pixels w pixel size 17.6 μm).
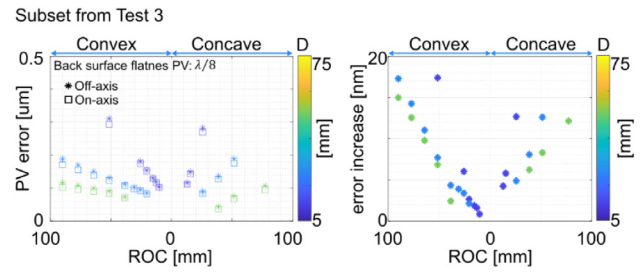

Fig. 24. (Test 6b) Comparison of the error when ignoring the off-center calibration procedure. Here we apply the telecentricity calibration parameter found for on-axis samples to on-axis samples (squares) and off-axis samples (asterisk).

Suppose the calibration parameter from a modeled on-axis sample is applied to an off-axis element (Fig. 24) with an offset between 1.5 and 2 pixels. In that case, the error increases by about 10% on convex samples with a 1″ diameter, and this value decreases with the aperture size.

To conclude the second telecentricity case (maximum telecentricity 0.1 instead 0.01), we only look at the reconstruction error introduced to a convex 0.5″ sample with a ROC of 51.5 mm, since this represents the worst case found for the lower telecentricity in Test 6b. For this configuration, the PV error is 443 nm. The error before calibration is 950 nm, and calibration without a misalignment error reduces this value to a PV of 300 nm; thus, the lateral misalignment for the larger telecentricity produces a relative change ∼48% or an increase of 143 nm.

3. DISCUSSION

Vision ray metrology (VRM) is a technique for measuring the wavefront of transparent optical samples by quantifying how light rays are deflected by the sample. This paper presents a new method to convert this wavefront information into the sample's surface height. The reconstruction method assumes that the front surface is solely responsible for the refraction of the rays, and therefore, any deviations from the flatness on the back surface can introduce errors in the calculation. We analyze the impact of these systematic errors, specifically those caused by the back surface flatness and imaging system telecentricity, on the accuracy of surface reconstruction.

Our findings provide practical insights and recommendations for the operation of VRM systems. For instance, we show that the telecentricity error may not be significant for small samples, but calibration becomes crucial for larger ones or for systems with larger telecentricity errors. For example, an increase of the sample diameter from 1" to 2" for a convex ROC increases the reconstruction PV error of the front surface between 3 and 4.4 times for Case A (telecentricity 0.1 deg) and between 2 and 3.5 times for Case B (telecentricity 0.01 deg). An increase of the telecentricity error (without calibration) from 0.01 to 0.1 deg can increase the error more than seven times for samples with D > 30 mm. On the other hand, small samples (D < 10 mm) only see an increase of a factor ∼2.

An interesting finding is that the telecentricity error disproportionately affects convex surfaces compared to concave surfaces, particularly with larger apertures. This is explained

by the impact on the telecentricity errors; the relative error in real deflected rays is greater for convex samples than for concave samples due to the change of diverging rays to converging rays. However, this effect lessens as the angle at which the outermost rays enter the sample decreases (i.e., as the sample size is reduced). In such cases, the difference in the error between concave and convex samples also becomes smaller. Consequently, we find that increasing the diameter from 1 to 2 in for concave samples approximately doubles the PV error in front surface reconstruction when the telecentricity is 0.1 deg (Case A). However, with a smaller telecentricity, the reconstruction is only slightly affected compared to when only the back surface flatness is considered. This suggests that concave surfaces are less susceptible to errors caused by the telecentricity, making them more robust to misalignment during calibration compared to convex surfaces. For convex surfaces, a 1 mm axial misalignment can result in a PV error close to 50 nm. In contrast, for concave surfaces with similar radii of curvature, the error is only around 20 nm, in the scenario with a telecentricity of 0.01 deg and the sample being close to the target. On the other hand, a lateral misalignment error produced a mixed behavior that depends on the slope of the front surface and the aperture size. Overall, for misalignments, a relative change in the reconstruction error of less than 20% is expected, with the concave samples and concave with the small ROC being more heavily affected. Nevertheless, larger telecentricity values make the calibration process more sensitive to misalignment errors, especially for larger samples, because the rays from the outermost part of the samples (with reference to the optical axis) have a larger telecentricity error.

While this manuscript focuses on specific systematic errors (back surface flatness and telecentricity), it is important to note that other potential error sources exist within the VRM system, such as the target flatness and linear stage errors during vision ray recovery. However, similar measurement setups also grapple with these errors, and advancements made by the metrology community to address them will undoubtedly benefit VRM as well.

4. CONCLUSION

This study advances vision ray metrology (VRM) [16] by introducing a novel method to convert wavefront information into the surface height and a calibration technique to mitigate telecentricity errors. Our findings provide practical guidance for using VRM systems, particularly in establishing tolerances for system alignment and highlighting the importance of calibration for larger samples.

While our approach simplifies front surface reconstruction, it does not capture the back surface, unlike transmission deflectometry systems such as [24]. However, deflectometry requires a complex calibration routine, and measurements commonly lead to significant low-frequency errors between a few hundred nanometers and 5 μm PV (first 12 Zernike polynomials) [26,33–35]. Hence, VRM is more accessible for high-precision metrology applications where back surface information is not critical.

This work also introduces a calibration technique to mitigate telecentricity errors, demonstrating submicron accuracy in surface reconstruction for samples with slow back surface slopes.

Additionally, we provide insights into the impact of misalignments, helping to set tolerances for system alignment. While this calibration significantly improves accuracy, the inherent flatness of the sample's back surface remains a limiting factor in precisely determining surface sag using vision ray metrology.

Disclosures. The authors declare no conflicts of interest.

Data availability. Data underlying the results presented in this paper are not publicly available at this time but may be obtained from the authors upon reasonable request.

REFERENCES AND NOTES

1. K. Falaggis, J. Rolland, F. Duerr, *et al.*, "Freeform optics: introduction," Opt. Express **30**, 6450–6455 (2022).
2. J. P. Rolland, M. A. Davies, T. J. Suleski, *et al.*, "Freeform optics for imaging," Optica **8**, 161–176 (2021).
3. J. Si, Z. Feng, D. Cheng, *et al.*, "Freeform beam splitting system design for generating an array of identical sub-beams," Opt. Express **29**, 29918–29935 (2021).
4. S. Shadalou and T. J. Suleski, "General design method for dynamic freeform optics with variable functionality," Opt. Express **30**, 19974–19989 (2022).
5. Z. Feng, D. Cheng, and Y. Wang, "Iterative freeform lens design for extended light source," Proc. SPIE **11895**, 1189506 (2021).
6. K. Creath and J. C. Wyant, "Use of computer-generated holograms in optical testing," in *Handbook of Optics* (1995), Vol. **2**, pp. 11–14.
7. R. Chaudhuri, A. Wansha, R. Porras-Aguilar, *et al.*, "Implementation of a null test for freeform optics using a high-definition spatial light modulator," Opt. Express **30**, 43938–43960 (2022).
8. T. Bothe, W. Li, M. Schulte, *et al.*, "Vision ray calibration for the quantitative geometric description of general imaging and projection optics in metrology," Appl. Opt. **49**, 5851–5860 (2010).
9. O. Huerta-Carranza, M. Avendaño-Alejo, and R. Díaz-Uribe, "Null screens to evaluate the shape of freeform surfaces: progressive addition lenses," Opt. Express **29**, 27921–27937 (2021).
10. J. DelOlmo-Márquez, G. Castillo-Santiago, M. Avendaño-Alejo, *et al.*, "Ronchi-Hartmann type null screens for testing a plano-freeform surface with a detection plane inside a caustic surface," Opt. Express **29**, 23300–23314 (2021).
11. O. Huerta-Carranza, M. Campos-García, F.-S. Granados-Agustín, *et al.*, "Simple method for evaluating plano-convex aspherical lenses," Proc. SPIE **12619**, 126190W (2023).
12. M. C. Knauer, J. Kaminski, and G. Hausler, "Phase measuring deflectometry: a new approach to measure specular free-form surfaces," Proc. SPIE **5457**, 366–376 (2004).
13. P. Su, R. E. Parks, L. Wang, *et al.*, "Software configurable optical test system: a computerized reverse Hartmann test," Appl. Opt. **49**, 4404–4412 (2010).
14. D. Wang, P. Xu, Z. Gong, *et al.*, "Transmitted wavefront testing with large dynamic range based on computer-aided deflectometry," J. Opt. - UK **20**, 065705 (2018).
15. T. Binkele, D. Hilbig, M. Essameldin, *et al.*, "Characterization of specular freeform surfaces from reflected ray directions using experimental ray tracing," J. Sens. Sens. Syst. **10**, 261–270 (2021).
16. A. H. Ramirez-Andrade, S. Shadalou, D. Gurganus, *et al.*, "Vision ray metrology for freeform optics," Opt. Express **29**, 43480–43501 (2021).
17. Imagine Optic, "HASO LIFT 680". https://www.imagine-optic.com/products/haso-lift-680-wavefront-sensor/.
18. PHASICS S.A, "SID4 HR," https://www.phasics.com/en/product/sid4-hr-wavefront-sensor/.
19. R. Wang, D. Li, W. Zheng, *et al.*, "Vision ray model based stereo deflectometry for the measurement of the specular surface," Opt. Lasers Eng. **172**, 107831 (2024).

20. J. Bartsch, Y. Sperling, and R. B. Bergmann, "Efficient vision ray calibration of multi-camera systems," Opt. Express **29**, 17125–17139 (2021).

21. S. Velghe, J. Primot, N. Guérineau, *et al.*, "Advanced wave-front sensing by quadri-wave lateral shearing interferometry," Proc. SPIE **6292**, 62920E (2006).

22. M. Mansuripur, "The Shack–Hartmann wavefront sensor," in *Classical Optics and its Applications* (Cambridge University, 2009), pp. 624–631.

23. L. Huang, J. Xue, B. Gao, *et al.*, "Modal phase measuring deflectometry," Opt. Express **24**, 24649–24664 (2016).

24. D. Wang, P. Xu, Z. Wu, *et al.*, "Simultaneous multisurface measurement of freeform refractive optics based on computer-aided deflectometry," Optica **7**, 1056–1064 (2020).

25. C. Wang, N. Chen, and W. Heidrich, "Towards self-calibrated lens metrology by differentiable refractive deflectometry," Opt. Express **29**, 30284–30295 (2021).

26. L. Yu, D. Li, Y. Ruan, *et al.*, "Wavefront aberration measurement deflectometry for imaging lens tests," Appl. Sci. **12**, 7857 (2022).

27. L. Jiang, X. Zhang, F. Fang, *et al.*, "Wavefront aberration metrology based on transmitted fringe deflectometry," Appl. Opt. **56**, 7396–7403 (2017).

28. D. Wang, Y. Yin, J. Dou, *et al.*, "Calibration of geometrical aberration in transmitted wavefront testing of refractive optics with deflectometry," Appl. Opt. **60**, 1973–1981 (2021).

29. H. Canabal, "Automatic wavefront measurement technique using a computer display and a charge-coupled device camera," Opt. Eng. **41**, 822–826 (2002).

30. FRED optical engineering software by Photon Engineering LLC.

31. Thorlabs Lens Catalog in Zemax OpticStudio 22.1.

32. M. Grenier, N. Desnoyers, F. Lamontagne, *et al.*, "Methods to achieve fast, accurate, and mechanically robust optical breadboard alignment," Opt. Eng. **60**, 051213 (2021).

33. L. R. Graves, H. Choi, W. Zhao, *et al.*, "Model-free deflectometry for freeform optics measurement using an iterative reconstruction technique," Opt. Lett. **43**, 2110–2113 (2018).

34. X. Zhang, Z. Niu, J. Ye, *et al.*, "Correction of aberration-induced phase errors in phase measuring deflectometry," Opt. Lett. **46**, 2047–2050 (2021).

35. A. Pouya Fard, "Low uncertainty surface area measurement using deflectometry," Dissertation (University of North Carolina at Charlotte, 2018).